frontiers | Frontiers in Energy Research

TYPE Original Research
PUBLISHED 19 August 2022
DOI 10.3389/fenrg.2022.918494

OPEN ACCESS

EDITED BY
Vivekanand Shukla,
Chalmers University of Technology, Sweden

REVIEWED BY
Ahmed I Osman,
Queen's University Belfast, United Kingdom
Yong Liu,
Henan University of Science and Technology, China

*CORRESPONDENCE
Tao Wen,
twen@ncepu.edu.cn

SPECIALTY SECTION
This article was submitted to Electrochemical Energy Conversion and Storage, a section of the journal Frontiers in Energy Research

RECEIVED 12 April 2022
ACCEPTED 18 July 2022
PUBLISHED 19 August 2022

CITATION
Wu B, Ma R, Liu X, Zheng Y, Guo S, Yi Y, Sun M, Wang S and Wen T (2022), Self-assembly synthesis of petal-like MoS_2/Co_9S_8/carbon nanohybrids for enhanced lithium storage performance. *Front. Energy Res.* 10:918494. doi: 10.3389/fenrg.2022.918494

Self-assembly synthesis of petal-like MoS_2/Co_9S_8/carbon nanohybrids for enhanced lithium storage performance

Bo Wu[1], Ran Ma[1], Xuewei Liu[1], Yuqi Zheng[1], Sisheng Guo[1], Yanmeng Yi[1], Mingtai Sun[2], Suhua Wang[1,2] and Tao Wen[1]*

[1]MOE Key Laboratory of Resources and Environmental Systems Optimization, College of Environment and Chemical Engineering, North China Electric Power University, Beijing, China, [2]Guangdong Provincial Key Laboratory of Petrochemical Pollution Process and Control, School of Environmental Science and Engineering, Guangdong University of Petrochemical Technology, Maoming, China

Transition metal sulfides are favored as anode materials for the next generation of lithium-ion batteries because of their high theoretical capacities and abundant natural resources. However, serious volume changes during charging and discharging pose great challenges to their stability. In this work, petal-like MoS_2/Co_9S_8/C nanohybrids were synthesized *via* the immobilization of molybdyl acetoacetonate $MoO_2(acac)_2$ in ZIF-67 and subsequent combined vulcanization and thermolysis process. Benefiting from the homogeneous bimetallic sulfide and highly conductive carbon layer, the as-obtained MoS_2/Co_9S_8/C nanohybrids exhibited a high initial discharge capacity of 988.3 mAh g^{-1} at 200 mA g^{-1} and a capacity retention > 99.9% after 50 cycles. Even at a high current density of 1000 mA g^{-1}, the reversible capacity of MoS_2/Co_9S_8/C is still as high as 754.6 mAh g^{-1}, revealing extraordinary rate ability. This work can provide a general approach to design and synthesize other advanced bimetallic chalcogenides for boosting lithium-ion batteries storage performance.

KEYWORDS

lithium-ion batteries, MoS_2/Co_9S_8/C nanohybrids, electrochemical performances, synergistic effect, self-assembly

Introduction

With the rapid increase in fossil energy consumption and ensuing environmental concerns, the development of clean and efficient energy storage is of great significance to fulfill the demands of higher specific energy, higher power density, and longer lifespan (Liu et al., 2012; Li et al., 2017; Chen et al., 2018a). Rechargeable lithium-ion batteries (LIBs) are a very appealing portable electronic device of energy conversion for large-scale applications (Zhou et al., 2015a; Wang et al., 2021; Miao et al., 2022). Nevertheless, the practical application of commercial graphite-based anodes have been frustrated due to their low theoretical capacity of 372 mAh g^{-1} (Zhou et al., 2014; Wang et al., 2017; Zhang et al., 2018). In the context of developing highly efficient energy storage electrode

materials, extensive research has been conducted on various advanced anode materials, including metal oxides, metal sulfides, and their composites (Ren et al., 2019; Tao et al., 2021). Recently, layer-structured transition metal chalcogenides (TMCs), such as MoS_2 (Jiang et al., 2015), Co_9S_8 (Liu et al., 2016), SnS (Ru et al., 2020), and FeS (Wang et al., 2018a), have become the limelight of research due to their high theoretical capacity, abundant natural resources, and environmental friendliness (Zhou et al., 2015b; Kim et al., 2020; Ke et al., 2021; Li et al., 2021).

Among those TMCs, molybdenum disulfide (MoS_2), in which S–Mo–S layers are held together by weak van der Waals forces, has received intensive research attention in lubrication, drug delivery, and energy storage due to its extraordinary activity and perfect two-dimensional structure (Maksoud et al., 2021). Particularly, MoS_2 is emerging as a potential candidate for lithium ion storage because of its excellent electrical, chemical, mechanical, and thermal properties (Hu et al., 2018). Excitingly, MoS_2 can uptake four Li ions during the lithiation process, corresponding to 669 mAh g^{-1} specific capacity, which is significantly higher than that of a commercial graphite anode (372 mAh g^{-1}) (Wang et al., 2016; Zhang et al., 2017). Unfortunately, the rapid capacity decay and poor rate performance of MoS_2 electrodes have greatly affected the commercialization of MoS_2 as an anode material (Wang et al., 2014; Yu et al., 2015). Numerous studies have been devoted to improve the intrinsic/ionic conductivity of MoS_2. In addition, the large volume excursion of MoS_2 brings about capacity fading during charge/discharge cycles (Chen et al., 2018b), and the higher surface energy and interlayer van der Waals forces of 2D materials leads to MoS_2 stacking, which further restricts its practical application (Zhang et al., 2015). In order to solve these issues, incorporation of other conductive materials with MoS_2 is considered as an effective way to achieve outstanding performance. For example, Fang et al. (2016) designed a vertically stacked ultrathin two-dimensional ordered mesoporous carbon/MoS_2–layered heterogeneous material with high reversible discharge capacity (1140 mAh g^{-1}) at a current density of 100 mA g^{-1}. Wu et al. (2019) synthesized a low-crystalline MoS_2 nanosheet encapsulated on nitrogen-doped carbon nanotubes (MoS_2/N-CNT), and the results showed that the material could reach 1003 mAh g^{-1} after 800 cycles at 2 A g^{-1}, demonstrating its high specific capacity and ultra-long cycle stability. In order to seek alternative anode materials, the combination of MoS_2 with other highly conductive sulfides, such as Co_3S_4 (Lei et al., 2018), SnS (Ru et al., 2020), and MnS (Chen et al., 2021), to form heterogeneous structures is also an important way to improve its electrochemical performance. Related studies have shown that the composites containing the MoS_2 component inherit the advantages of each component. In other words, MoS_2-based composites synergistically improve the electrochemical kinetics and structural stability, thus offering superior electrochemical performance and commercialization prospects (Yang et al., 2020). Taking the aforementioned issues into account, the rational design of MoS_2, carbon, and other metal sulfides could synergistically promote the electronic conductivity of nanohybrids and reduce the bulk effect during cycling.

Metal organic frameworks (MOFs), an emerging class of functional nanomaterials, possess outstanding tunable nanostructures, high porosity, and large specific surface area, making them ideal carbon matrixes for electrode materials (Aslam et al., 2018; Huang et al., 2021). Furthermore, such assembly of metal ions/clusters with organic linkers offers prospective application in catalysis, energy storage, and other fields (Fu et al., 2021; Tu et al., 2021). Encouragingly, serving as sacrificial templates, the reactive metal components embedded in MOFs could be transformed *in situ* into metal sulfides after vulcanization reaction, while the organic ligands are converted to amorphous carbon during the annealing treatment. The metal sulfides/carbon composite–derived MOFs would be favored for their excellent electrochemical properties due to their porous nanostructures. Recently, Guo et al. (2020) reported a strategy using zeolitic imidazolate framework 67 (ZIF-67) as a precursors to prepare the Co_9S_8/C anode material, delivering a specific capacity of 700 mAh g^{-1} at a current density of 500 mA g^{-1} after 150 cycles. Note that Co_9S_8 owns high theoretical capacity (545 mAh g^{-1}), low cost, outstanding electrical conductivity, and superior thermal stability (Huang et al., 2020). However, to date, there have been few studies on coupling with layered MoS_2 and MOF-derived other metal sulfides/carbon ingredients, which are capable in enhancing the electrochemical performances in LIBs.

The objectives of this study are 1) to synthesize MoS_2/Co_9S_8/C nanohybrids *via* the coordination-driven self-assembly of molybdyl acetoacetonate [$MoO_2(acac)_2$] into ZIF-67, followed by an *in situ* vulcanization strategy and finally a thermal annealing process; 2) to characterize the physicochemical properties of MoS_2/Co_9S_8/C using various techniques; and 3) to estimate the lithium storage performance as anode materials in LIBs. In this approach, thanks to the advantage of ZIF-67's unique hydrocarbon networks, bimetal sulfides could be simultaneously converted to MoS_2/Co_9S_8 embedded in the carbon matrix (MoS_2/Co_9S_8/C), which effectively prevented aggregation of the ZIF-67–derived sulfides. This unique structure is able to act as a buffer to mitigate severe volume changes during charging/discharging. In addition, the synergistic effect of MoS_2, Co_9S_8, and carbon not only imparts excellent electrical conductivity and high structural stability but also promotes electron/ion transfer and reaction kinetics. As expected, in comparison with individual bulk MoS_2 and Co_9S_8/C, the MOF-derived MoS_2/Co_9S_8/C exhibited excellent lithium storage performance as anode materials in LIBs, maintaining a capacity of 1270.2 mAh g^{-1} at a current density of 100 mA g^{-1} and a remarkable rate capability of 754.6 mAh g^{-1}

at 1000 mA g^{-1}. Their synergy endows MOF-derived multiple metal sulfides favorable for the effective storage of lithium ions.

Experimental section

Chemicals

All chemicals used in the experiments were obtained from commercial sources and were not further purified before use. Molybdyl acetoacetonate [$MoO_2(acac)_2$, 97%], 2-methylimidazole (98%), and cobalt nitrate hexahydrate [$Co(NO_3)_2{\cdot}6H_2O$, 99%] were purchased from Shanghai Aladdin Bio-Chem Technology Co., Ltd. Ammonium molybdate tetrahydrate ($(NH_4)_6Mo_7O_{24}{\cdot}4H_2O$, 99%) and thioacetamide (TAA, 99%) were supplied by Shanghai Macklin Bio-Chem Technology Co., Ltd.

Materials synthesis

Synthesis of $MoO_2(acac)_2$/ZIF-67: 5 g of $MoO_2(acac)_2$ and 3.49 g of $Co(NO_3)_2{\cdot}6H_2O$ were first dissolved in 100 ml of absolute methanol. Afterward, 3.94 g of 2-methylimidazole was dissolved in another 100 ml of absolute methanol to generate a clear solution. Subsequently, both the solutions were mixed together in a flask and then kept at 60°C for 24 h. The product was separated by centrifugation and washed with methanol several times. Finally, the obtained $MoO_2(acac)_2$/ZIF-67 powder was dried and stored in a vacuum oven at 60°C for 12 h.

Synthesis of MoS_2/Co_9S_8/C: In a typical procedure, 180 mg of $MoO_2(acac)_2$/ZIF-67 and 360 mg of TAA were ultrasonically dispersed in 30 ml of ultrapure water, and then the solution was transferred to a teflon-lined stainless steel autoclave and kept at 220°C for 18 h. After cooling down, the black product was collected by centrifugation, washed five times with ultrapure water and then once with ethanol, and finally dried under vacuum at 60°C for overnight. The obtained MoCoS powders were directly annealed under N_2 atmosphere at 800 C for 2 h with a ramping rate of 5°C min^{-1}. The individual MoS_2 and Co_9S_8/C samples were fabricated according to the typical vulcanization reaction of $(NH_4)_6Mo_7O_{24}{\cdot}4H_2O$ or ZIF-67 with TAA under identical condition.

Characterization

The crystal structures of the materials were analyzed by X-ray diffraction (XRD, Rigaku SmartLab SE) using Cu Kα radiation (λ = 1.5406 Å) with a sweep rate of 10°/min. The morphological characterizations of the samples were performed by a scanning electron microscope (SEM, Thermo Fisher Scientific, Quattro). The transmission electron microscopy (TEM) and energy-dispersive X-ray spectroscopy (EDS) images were performed on a Hitachi H-7650 microscope. The X-ray photoelectron spectroscopy (XPS) measurements were performed using a PerkinElmer IR-843 spectrometer. According to the Barrett Joyner Halenda (BJH) model, the pore size distributions were tested by using the TriStar II 3020 analyzer. A thermogravimetric analysis (TGA) was investigated under air atmosphere from indoor temperature to 700°C on a NETZSCH STA 2500 thermal gravimetric analyzer.

Electrochemical measurement

The working electrodes were prepared by mixing active materials (MoS_2, Co_9S_8/C, and MoS_2/Co_9S_8/C), conductive agent carbon black, binder polyvinylidene difluoride in the ratio of 8:1:1 with appropriate amount of N-methyl-2-pyrrolidinone. Then the mixture was coated on the copper foil and dried at 80°C under vacuum for 12 h. Lithium metal disks worked as the counter/reference electrode, and the solution of 1.0 M $LiPF_6$ in a 1:1:1 volume ratio of ethylene carbonate (EC), diethyl carbonate (DEC), and ethyl methyl carbonate (EMC) was employed as the electrolyte for the cells. We assembled CR2032 type coin cells in a glove box filled with argon and used them for various electrochemical tests. The galvanostatic charge/discharge behaviors of the batteries were tested at different current densities from 0.01–3.0 V with the LAND battery test system. Cyclic voltammetry (CV) and electrochemical impedance spectroscopy (EIS) were tested using an electrochemical workstation (Metrohm AG, PGSTAT302N). CV curves were collected at a scan rate of 0.1 mV s^{-1} from 0.01 to 3.0 V, and EIS data were performed at the frequency range from 100 kHz to 10 mHz with an amplitude of 5 mV. In the calculated specific capacities, the composited electrodes were based on the total mass of MoS_2, Co_9S_8/C, or MoS_2/Co_9S_8/C nanohybrids.

Results and discussion

Morphologies and microstructures of the nanocomposites

The synthetic route of petal-like MoS_2/Co_9S_8/C nanohybrids is depicted in Figure 1. First, we prepared ZIF-67–wrapped $MoO_2(acac)_2$ as a precursor by introducing Mo source during ZIF-67 generation. Then a bimetallic sulfide was synthesized by hydrothermal vulcanization of the as-obtained $MoO_2(acac)_2$/ZIF-67 particles in the presence of TAA. Finally, in order to improve the electrical conductivity and crystallinity of the sulfide, the composites were heated under N_2 atmosphere at 800°C for 2 h. During the process of thermal carbonization, amorphous

FIGURE 1
Schematic illustration of the formation process of the petal-like $MoS_2/Co_9S_8/C$ nanohybrids.

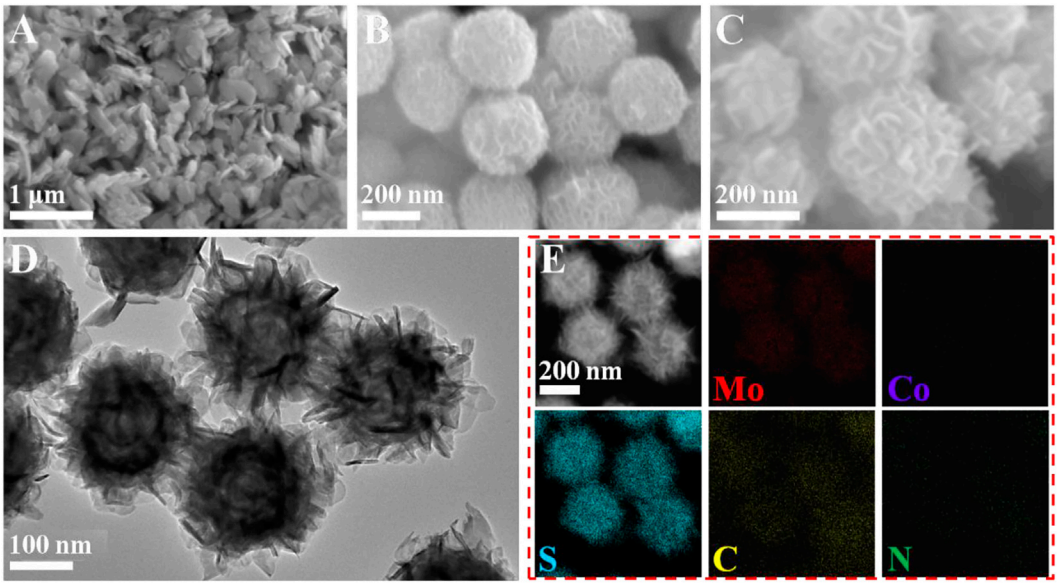

FIGURE 2
(A–C) SEM images of $MoO_2(acac)_2$/ZIF-67, MoCoS, and $MoS_2/Co_9S_8/C$ composites. **(D)** TEM image of $MoS_2/Co_9S_8/C$. **(E)** TEM image of $MoS_2/Co_9S_8/C$ and the corresponding elemental mapping images of Mo, Co, S, C, and N.

CoS was converted to Co_9S_8, accompanying with the transformation *in situ* of organic moiety into a more conductive carbon layer. As a result, $MoS_2/Co_9S_8/C$ nanohybrids can be eventually achieved.

The morphologies of the aforementioned materials at different stages were determined by scanning electron microscopy (SEM) and transmission electron microscopy (TEM). From the SEM image of the precursor $MoO_2(acac)_2$/ZIF-67 (Figure 2A), one can see that $MoO_2(acac)_2$/ZIF-67 consisted of irregular nanoplatelets, which are clearly different from the typical polyhedral structure of ZIF-67 (Supplementary Figure S1A). This phenomenon was mainly attributed that the presence of $MoO_2(acac)_2$ in the reaction interferes the pairing of 2-methylimidazole with cobalt ions, thus preventing the formation of the well-defined polyhedron structure. When undergoing hydrothermal vulcanization, in which the $MoO_2(acac)_2$/ZIF-67 nanosheets self-assembled into nanospheres, the intermediate MoCoS exhibits a uniform petal-like nanostructure with a diameter of about 300 nm (as shown in Figure 2B). From Figure 2C, we can observe that after thermal annealing treatment, $MoS_2/Co_9S_8/C$ nanohybrids maintained the original petal-like structure without any damage in morphology. Also, for comparison, bulk MoS_2 and Co_9S_8/C were further synthesized, as shown in Supplementary Figure S1A, S2.

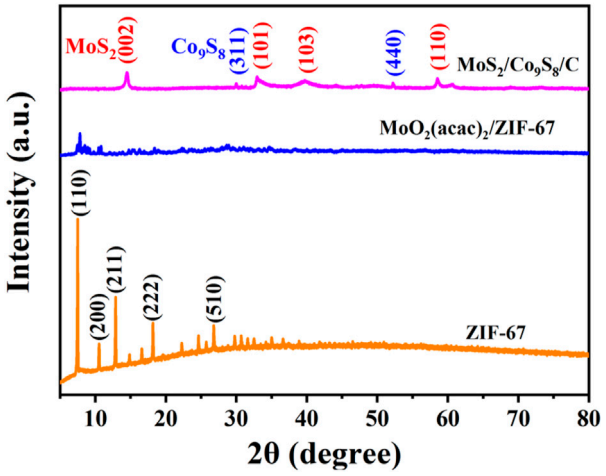

FIGURE 3
XRD patterns of ZIF-67, $MoO_2(acac)_2$/ZIF-67, and MoS_2/Co_9S_8/C nanohybrids.

Apparently, Co_9S_8/C derived from ZIF-67 retained the former polyhedral structure. However, the as-synthesized Co_9S_8/C underwent some agglomeration, while the individual MoS_2 exhibited a classical blocky structure. Moreover, the SEM images of both MoS_2 and Co_9S_8/C showed several microns in size. Compared with MoS_2 and Co_9S_8/C, MoS_2/Co_9S_8/C nanohybrids assembled by thin layers greatly increase the contact area between electrode and electrolyte and shorten the lithium ion transport path (Yang et al., 2020). In addition, such a special structure of nanospherical shape would play a positive role in alleviating the severe volume change during the charging/discharging process (Hu et al., 2018). These results suggested that synthesized MoS_2/Co_9S_8/C nanohybrids would be capable of implementing a good Li^+ storage performance when used as the anode of LIBs. As observed from Figure 2D, the TEM image further demonstrated that MoS_2/Co_9S_8/C nanohybrids were assembled from a series of nanosheets into petal-like nanospheres. As shown in Figure 2E, energy-dispersive X-ray spectroscopy (EDS) mappings of MoS_2/Co_9S_8/C revealed the homogeneous distribution of Mo, Co, S, C, and N throughout the whole nanohybrids, indicating that $MoO_2(acac)_2$ species was uniformly encapsulated in ZIF-67 when the cobalt ion was paired with 2-methylimidazole to form ZIF-67.

X-ray diffraction (XRD) was used to identify the crystallographic structure of these samples derived at different stages. As shown in Figure 3, the diffraction peaks of the synthesized ZIF-67 could be readily indexed to the reported patterns of the ZIF-67 crystal (Yang et al., 2018). The XRD pattern of $MoO_2(acac)_2$/ZIF-67 were similar to that of pristine ZIF-67, and the presence of $MoO_2(acac)_2$ dramatically interfered the formation of well-defined nucleation and growth of ZIF-67 crystals, resulting in the relative low intensity in the XRD pattern of $MoO_2(acac)_2$/ZIF-67. After vulcanization and calcination processes (Figure 3), the characteristic peaks located at 14.4°, 33.4°, 39.5°, 44.2°, 58.2°, and 60.3° were related to the (002), (101), (103), (104), (110), and 112) reflections of a typical hexagonally structural MoS_2 (JCPDS No. 37–1492) (Geng et al., 2017). While the diffraction peaks at 29.9° and 52.0° correspond to (311) and (440) planes of face centered cubic Co_9S_8 (JCPDS No. 65–6801) (Geng et al., 2017). These results implied that the metal chalcogenide hybrids are the mixture of MoS_2 and Co_9S_8 without other phases, revealing the high purity of the product.

The amount of carbon component in MoS_2/Co_9S_8/C nanohybrids was determined by a thermogravimetric analysis (TGA). From Figure 4A, we can clearly see that there were three weight loss processes in the TGA analysis of MoS_2/Co_9S_8/C. The first weight loss was started from room temperature to 180°C, which can be attributed to the evaporation or desorption of physically adsorbed water. The second weight loss of the sample occurred at 180–482°C, which is due to the oxidation of the metal sulfides by O_2 in the air. Ultimately, as the temperature continues to rise, the decomposition of carbon in MoS_2/Co_9S_8/C nanohybrids is accompanied by releasing of CO_2 (Ren et al., 2019). The result of TGA curve showed that the carbon mass percentage in MoS_2/Co_9S_8/C was about 6.1%. The pore distribution of MoS_2/Co_9S_8/C nanohybrids was investigated by N_2 adsorption and desorption analysis. The corresponding pore size distribution calculated by the Barrett Joyner Halenda (BJH) method displayed a narrow distribution centered at 3.3 nm in diameter.

The chemical constituents and valance information of MoS_2/Co_9S_8/C nanohybrids were further analyzed by X-ray photoelectron spectroscopy (XPS). As shown in Figure 5A, the survey spectrum confirmed that Mo 3d, Co 2p, S 2p, C 1s, N 1s, and O 1s peaks exist in the sample of MoS_2/Co_9S_8/C nanohybrids. From the high-resolution XPS spectrum of Mo 3d (Figure 5B), the binding energies located at 229.8, 232.9, and 226.9 eV originated from Mo $3d_{5/2}$, Mo $3d_{3/2}$, and S 2s, respectively (Wang et al., 2018b), implying the presence of Mo^{4+} species and the formation of MoS_2 in the composites. Meanwhile, a broad peak at 235.7 eV of Mo^{6+} was indicative of the existence of oxidized phases (i.e., Mo^{6+}) (Hou et al., 2018). As observed from Figure 5C, two pairs of peaks were the features of Co^{2+} (Co $2p_{1/2}$ at 799.5 eV and Co $2p_{3/2}$ at 782.8 eV) and Co^{3+} (Co $2p_{1/2}$ at 788 eV and Co $2p_{3/2}$ at 779.6 eV) (Ren, et al., 2019). Moreover, two peaks located at 804.4 and 784.8 eV were the shakeup satellites (Hou et al., 2018). Combined with the core level of the S 2p spectrum (Figure 5D), the characteristic peaks of S $2p_{3/2}$ at 162.6 eV and S $2p_{1/2}$ at 163.8 eV were attributed to S^{2-} of both Co-S and Mo-S bonds, and the shakeup satellite peak in 169.6 eV might be ascribed to the partial surface oxidization (Geng et al., 2017). The region of C 1s spectrum could be grouped into three components originating from centered at C-C (284.7 eV), C-N (285.7 eV), and C=O bonds (287.4 eV), respectively, as displayed in Figure 5E, while the N 1s XPS

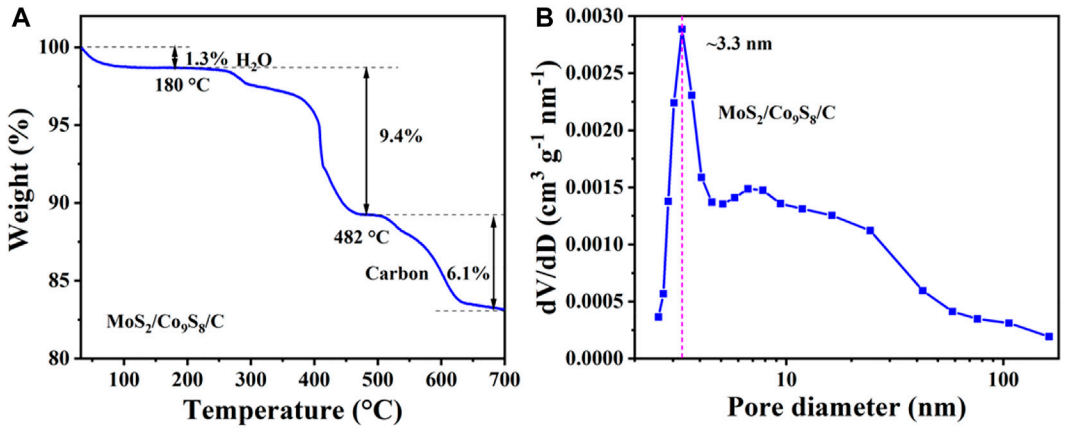

FIGURE 4
(A) Thermogravimetric data of $MoS_2/Co_9S_8/C$ powder sample in air atmosphere. **(B)** Pore size distributions of $MoS_2/Co_9S_8/C$.

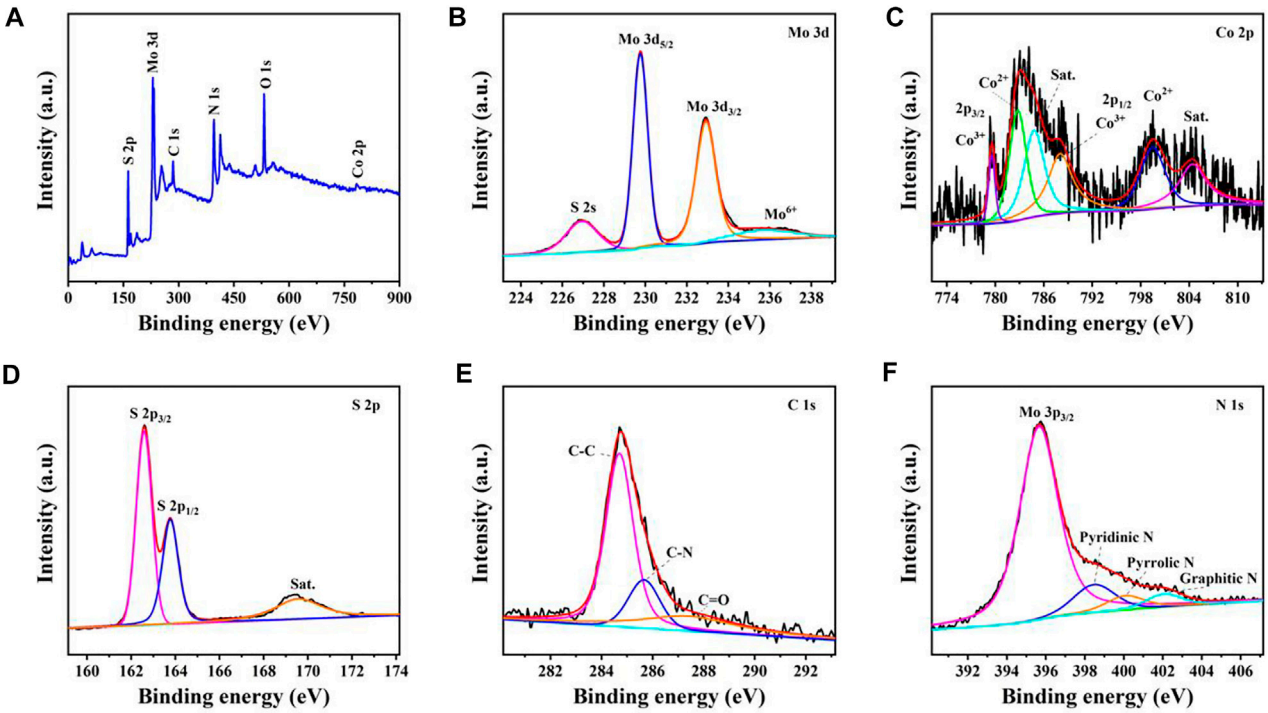

FIGURE 5
XPS spectra of $MoS_2/Co_9S_8/C$ nanohybrids: **(A)** survey spectrum, **(B)** Mo 3d, **(C)** Co 2p, **(D)** S 2p, **(E)** C 1s, and **(F)** N 1s.

spectrum of $MoS_2/Co_9S_8/C$ could be fitted into four peaks, which are associated with the Mo 3p (395.6 eV), pyridinic N (398.5 eV), pyrrolic N (400 eV), and graphitic N (402.1 eV) (Zhao et al., 2018). The result of XPS spectra survey demonstrated the formation of heterostructures between Co_9S_8 and MoS_2.

Electrochemical performances

The anodic electrochemical performance of $MoS_2/Co_9S_8/C$ nanohybrids in LIBs was systematically evaluated by assembling a series of half-cells. Figures 6A–C showed the cyclic

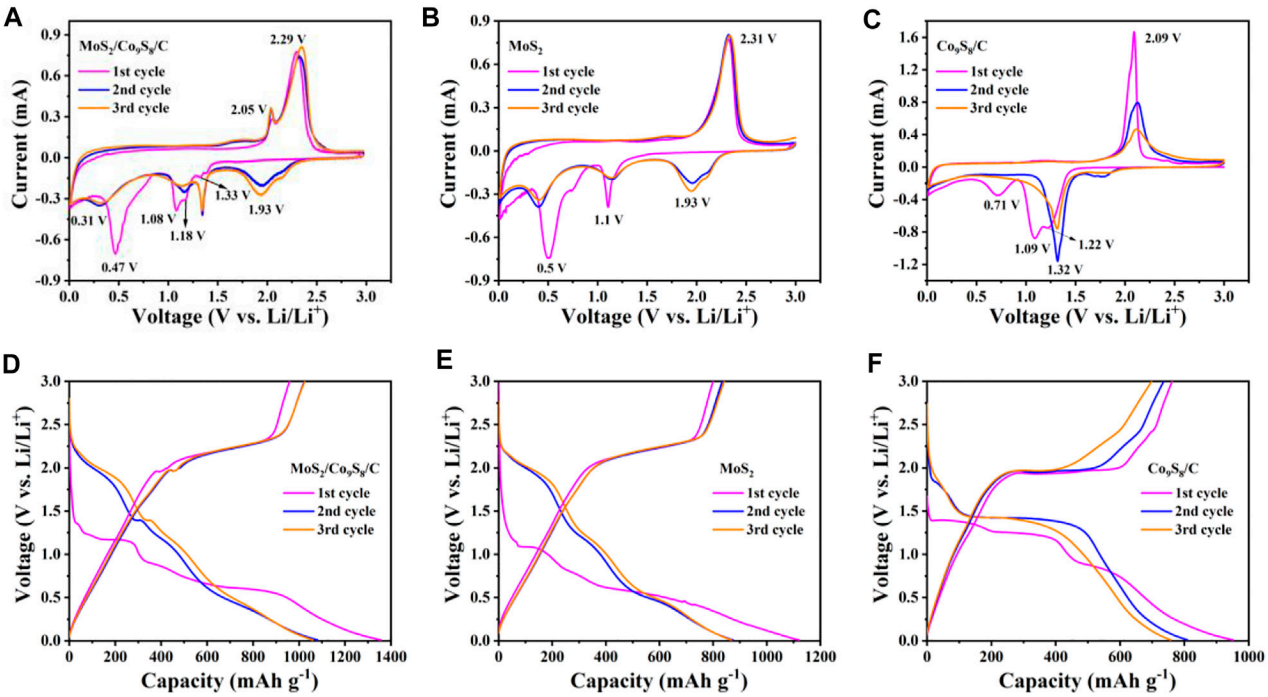

FIGURE 6
(A–C) CV curves of $MoS_2/Co_9S_8/C$, MoS_2, and Co_9S_8/C electrodes at a scanning rate of 0.1 mV s^{-1} during the initial three cycles. **(D–F)** Galvanostatic discharge/charge profiles of $MoS_2/Co_9S_8/C$, MoS_2, and Co_9S_8/C electrodes at 100 mA g^{-1}.

voltammetry (CV) curves of $MoS_2/Co_9S_8/C$, MoS_2, and Co_9S_8/C electrodes for the first three cycles at a scanning rate of 0.1 mV s^{-1} and a voltage range of 0.01–3.0 V. As shown in Figure 6A, in the first cathode scan, we can observe that $MoS_2/Co_9S_8/C$ has four reduction peaks at 0.47, 1.08, 1.18, and 1.33 V, respectively, revealing a multistep electrochemical reaction. The two peaks located at 1.18 and 1.33 V can be ascribed to the reduction of Co_9S_8 to metallic Co (Zhao et al., 2018; Ren et al., 2019). Also, the strong peak at 1.08 V is the result of the intercalation of lithium ions into the MoS_2 layer, while the pronounced reduction peak at 0.47 V in the first cycle was identified to the reduction of Li_xMoS_2 and the formation of a solid electrolyte interphase (SEI) layer (Ren et al., 2019). During the reverse anodic sweep of the $MoS_2/Co_9S_8/C$, two intensive peaks at 2.05 and 2.29 V could be attributed to the oxidation of metallic Co and Mo, respectively (Geng et al., 2017). In the following CV cycle, the lithium ion storage mechanism of MoS_2 turns into a reversible redox reaction of sulfur (Yang et al., 2020). The overlapped of the second and third cycles also demonstrated that Li^+ ions could be reversibly inserted into and extracted from $MoS_2/Co_9S_8/C$ nanohybrids. The CV curves of individual MoS_2 and Co_9S_8/C electrodes were also investigated for comparison. As shown in Figure 6B, two reduction peaks at 0.5 and 1.1 V can be attributed to the embedding of lithium ions and the reduction of Li_xMoS_2, respectively, while the three reduction peaks located at 0.71, 1.09, and 1.22 V in Figure 6C were the result of the reduction of Co_9S_8 to metallic Co. The oxidation peaks of MoS_2 at 2.31 V and Co_9S_8 at 2.09 V were assigned to the oxidation peaks of MoS_2 and Co_9S_8. These results indicated that MoS_2 and Co_9S_8 exhibited synergistic effects in $MoS_2/Co_9S_8/C$ nanohybrids, which would contribute to good reversibility and cyclic stability together with boosting LIBs storage.

These corresponding plateaus were further observed in the galvanostatic charge/discharge profiles of the $MoS_2/Co_9S_8/C$ nanohybrids, MoS_2 and Co_9S_8/C at a current density of 100 mA g^{-1} within the voltage window of 0.01–3.0 V (vs. Li/Li^+) (Figures 6D–F). For the $MoS_2/Co_9S_8/C$ electrode, the initial discharge/charge capacities achieved 1356.5 and 958.9 mA h g^{-1}, respectively, higher than those of MoS_2 (1121.2 and 800 mAh g^{-1}) and Co_9S_8/C (951.1 and 762.2 mAh g^{-1}). The corresponding initial Coulombic efficiencies (CEs) of $MoS_2/Co_9S_8/C$, MoS_2 and Co_9S_8/C reached up to ~70.69%, ~71.35 and ~80.14%, respectively. After the initial adjustment cycle, petal-like nanospheres–structured $MoS_2/Co_9S_8/C$ delivered the highest discharge/charge capacities and stability compared to those of MoS_2 and Co_9S_8/C in the 2nd and 3rd cycles. More importantly, by comparing the charge/discharge curves and CV curves of $MoS_2/Co_9S_8/C$, it was found that $MoS_2/Co_9S_8/C$ brought two charging and multiple discharge plateaus, which were consistent with the result in the CV profile of $MoS_2/Co_9S_8/C$.

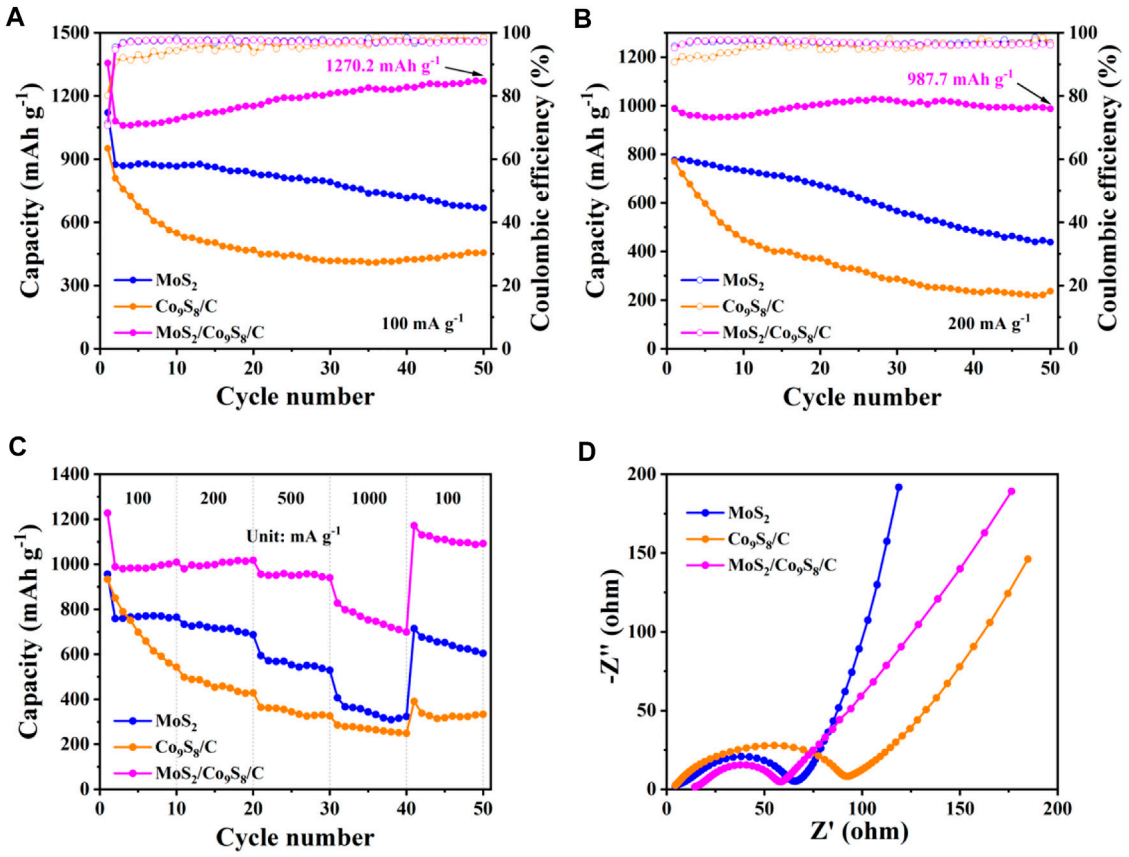

FIGURE 7
Cycling performance together with Coulombic efficiency of $MoS_2/Co_9S_8/C$, MoS_2, and Co_9S_8/C at a current density of **(A)** 100 mA g^{-1} and **(B)** 200 mA g^{-1}, respectively. **(C)** Rate capability performance of $MoS_2/Co_9S_8/C$, MoS_2, and Co_9S_8/C. **(D)** Nyquist plots of $MoS_2/Co_9S_8/C$, MoS_2, and Co_9S_8/C in the frequency range between 100 kHz and 10 mHz.

The long-term cycling performance and coulombic efficiencies (CEs) of the $MoS_2/Co_9S_8/C$, MoS_2 and Co_9S_8/C were subsequently explored at a current density of 100 mA g^{-1} between 0.01 and 3.0 V. From Figure 7A, one can see that the discharge capacities of $MoS_2/Co_9S_8/C$, MoS_2 and Co_9S_8/C after 50 charge/discharge cycles were 1270.2, 668.5, and 455.3 mAh g^{-1}, presenting 93.64%, 59.62% and 47.87% retention of 50th discharge capacity. Furthermore, Figure 7B further displayed the compared cycling performance of $MoS_2/Co_9S_8/C$, MoS_2 and Co_9S_8/C electrodes at a higher current density of 200 mA g^{-1}. It was found that the initial discharge capacities of $MoS_2/Co_9S_8/C$, MoS_2 and Co_9S_8/C were 988.3, 776.3, and 770.6 mAh g^{-1}, respectively. After 50 cycles, the discharge capacities of MoS_2 and Co_9S_8/C faded to 438.6 and 236.7 mAh g^{-1}, respectively. Surprisingly, $MoS_2/Co_9S_8/C$ possessed a remarkable discharge capacity of 987.7 mAh g^{-1} after 50 cycles, which was almost 2.25 times of that of the bare MoS_2 and 4.17 times of that of the Co_9S_8/C. Notably, the CE of $MoS_2/Co_9S_8/C$ approached nearly 100% throughout the overall cycle. These results fully proved that the $MoS_2/Co_9S_8/C$ nanohybrids' capacity and cyclability were significantly higher than the MoS_2 and Co_9S_8/C. Furthermore, the high specific capacity (1270.2 mAh g^{-1}) at 100 mA g^{-1} was achieved for $MoS_2/Co_9S_8/C$ nanohybrids by comparison with most reported MoS_2-based anode materials. Surprisingly, the ternary $MoS_2/Co_9S_8/C$ nanohybrids present better lithium storage performances than previous bare MoS_2 and MoS_2/carbon composites, indicating that integrating $MoS_2/Co_9S_8/C$ nanohybrids with hierarchical structure could offer a scalable approach to develop promising anode materials for LIBs.

Figure 7C showed the rate performance comparison of these three electrodes at different current densities ranging from 100 to 1000 mA g^{-1}. Upon comparison of the MoS_2 and Co_9S_8/C electrodes, the $MoS_2/Co_9S_8/C$ nanohybrids delivered superior capacities and improved rate performance, with average discharge capacities of 1013.8, 1002.9, 951.4, and 754.6 mAh g^{-1} at current densities of 100, 200, 500, and 1000 mA g^{-1}, respectively. Note that the discharge capacity of $MoS_2/Co_9S_8/C$ could recover to 1112.2 mAh g^{-1} as the current density returned to 100 mA g^{-1}, which was higher than the capacity after 10 cycles at 100 mA g^{-1} initially. Meanwhile, the discharge capacities of $MoS_2/Co_9S_8/C$

TABLE 1 Lithium storage performances of the present $MoS_2/Co_9S_8/C$ with the reported MoS_2-based anode materials.

Materials	Specific capacity (mAh g^{-1})	Cycling number	Current rate (mA g^{-1})	References
MoS_2 nanoflowers	814	50	100	Lu, et al. (2015)
Layer-controlled MoS_2/graphene aerogels	573	50	100	Zhao et al. (2016)
Nitrogen-doped carbon-embedded MoS_2 microspheres	1055	100	150	Xie et al. (2016)
Hierarchical MoS_2 shells supported on carbon spheres	750	50	100	Zhang and Lou, (2014)
MoS_2-multiwalled carbon nanotube hybrids	1090	30	100	Bindumadhavan et al. (2013)
MoS_2 nanosheets grown on grapheme sheets	1077	150	100	Teng, et al. (2016)
$MoS_2/Co_9S_8/C$ nanohybrids	1270.2	50	100	This work

were much higher than those of MoS_2 and Co_9S_8/C at any current densities, and the bare MoS_2 and Co_9S_8/C electrodes only maintained discharge capacities of 323.6 and 249 mAh g^{-1} at high rate of 1000 mA g^{-1}. Such enhanced rate performance of high power output was mainly attributed to the integrating features of $MoS_2/Co_9S_8/C$ nanohybrids: 1) the unique petal-like structure promoted the fast electronic transportation in the bulk electrode, 2) the carbon layer preserved the reactive surface and high conductivity, 3) the MoS_2 and Co_9S_8 active materials contributed to the high capacity.

To understand the enhanced rate capability, resistance of three electrodes was further tested by electrochemical impedance spectroscopy (EIS). All the assembled batteries were cycled once at a current density of 100 mA g^{-1} prior to EIS testing. The Nyquist plots of the cells assembled with the three materials were shown in Figure 7D, and each curve was composed of a semicircle and a straight line, where the size of the semicircle reflected the magnitude of the charge transfer impedance (Rct) between the electrolyte and the electrode (Ke et al., 2021). Clearly, the Rct value of $MoS_2/Co_9S_8/C$ is the smallest relative to that of Co_9S_8/C and MoS_2, indicating that the reaction speed of $MoS_2/Co_9S_8/C$ is faster in the process of lithium intercalation/delamination (Zhao et al., 2020). This also confirmed that in the $MoS_2/Co_9S_8/C$ nanohybrids, there is a synergistic effect between MoS_2 and Co_9S_8/C, resulting in enhanced electrochemical cycling and rate properties (Han et al., 2020).

Conclusion

In conclusion, we have rationally designed and successfully prepared petal-like $MoS_2/Co_9S_8/C$ nanohybrids by a simple self-assembly approach. This unique structure can not only buffer the huge volume change of the electrode during the charging/discharging process of LIBs but also greatly shorten the electron and ion transfer pathway and promote the kinetics of the reaction. In addition, the synergistic effect between MoS_2 and Co_9S_8 embedded in the carbon matrix significantly imparts to $MoS_2/Co_9S_8/C$ outstanding lithium storage capacity, conductivity, and stability. Excitingly, when serving as the anode of LIBs, $MoS_2/Co_9S_8/C$ delivers a high reversible specific capacity of 1270.2 mAh g^{-1} at 100 mA g^{-1} after 50 cycles, which is a significant improvement compared to those of MoS_2 electrode (668.5 mAh g^{-1}) and Co_9S_8/C electrode (455 mAh g^{-1}). Moreover, the nanohybrids display superior average discharge capacities of 1013.8, 1002.9, 951.4, and 754.6 mAh g^{-1} at current densities of 100, 200, 500, and 1000 mA g^{-1}, respectively. These integrating features demonstrate that the synthesized petal-like $MoS_2/Co_9S_8/C$ nanohybrids would be capable in boosting the lithium storage performance. In the future research directions, we will devote to investigating the intelligent synthetic process and exploring the *in situ* galvanostatic discharge/charge process using advanced spectroscopic techniques (Table 1).

Data availability statement

The original contributions presented in the study are included in the article/Supplementary Material; further inquiries can be directed to the corresponding author.

Author contributions

BW performed the most experiments and wrote the manuscript. RM and XL performed partial experiments. YZ and SG performed data analysis. YY plotted the figures. MS designed the experiments. SW edited the manuscript. TW proposed the project and revised the manuscript.

Funding

This work was financially supported by the National Key Research and Development Program of China (2018YFC1900105), Science Challenge Project (TZ2016004), and Beijing Outstanding Young Scientist Program.

Conflict of interest

The authors declare that the research was conducted in the absence of any commercial or financial relationships that could be construed as a potential conflict of interest.

Publisher's note

All claims expressed in this article are solely those of the authors and do not necessarily represent those of their affiliated organizations, or those of the publisher, the editors, and the reviewers. Any product that may be evaluated in this article, or claim that may be made by its manufacturer, is not guaranteed or endorsed by the publisher.

Supplementary material

The Supplementary Material for this article can be found online at: https://www.frontiersin.org/articles/10.3389/fenrg.2022.918494/full#supplementary-material

References

Aslam, M. K., Shah, S. S. A., Li, S., and Chen, C. (2018). Kinetically controlled synthesis of MOF nanostructures: Single-holed hollow core-shell ZnCoS@Co_9S_8/NC for ultra-high performance lithium-ion batteries. *J. Mat. Chem. A* 6, 14083–14090. doi:10.1039/c8ta04676j

Bindumadhavan, K., Srivastava, S. K., and Mahanty, S. (2013). MoS_2–MWCNT hybrids as a superior anode in lithium-ion batteries. *Chem. Commun.* 49 (18), 1823–1825. doi:10.1039/c3cc38598a

Chen, B., Lu, H., Zhou, J., Ye, C., Shi, C., Zhao, N., et al. (2018a). Porous MoS_2/carbon spheres anchored on 3D interconnected multiwall carbon nanotube networks forUltrafast Na storage. *Adv. Energy Mat.* 8, 1702909. doi:10.1002/aenm.201702909

Chen, C., Xie, X., Anasori, B., Sarycheva, A., Makaryan, T., Zhao, M., et al. (2018b). MoS_2-on-MXene heterostructures as highly reversible anode materials for lithium-ion batteries. *Angew. Chem. Int. Ed.* 57, 1846–1850. doi:10.1002/anie.201710616

Chen, F., Shi, D., Yang, M., Jiang, H., Shao, Y., Wang, S., et al. (2021). Novel designed MnS-MoS_2 heterostructure for fast and stable Li/Na storage:insights into the advanced mechanism attributed to phase engineering. *Adv. Funct. Mat.* 31, 2007132. doi:10.1002/adfm.202007132

Fang, Y., Lv, Y., Gong, F., Elzatahry, A. A., Zheng, G., and Zhao, D. (2016). Synthesis of 2D-mesoporous-carbon/MoS_2 heterostructures with well-defined interfaces for high-performance lithium-ion batteries. *Adv. Mat.* 28, 9385–9390. doi:10.1002/adma.201602210

Fu, L., Kang, C., Xiong, W., Tian, P., Cao, S., Wan, S., et al. (2021). WS_2 nanosheets@ZIF-67-derived N-doped carbon composite as sodium ion battery anode with superior rate capability. *J. Colloid Interface Sci.* 595, 59–68. doi:10.1016/j.jcis.2021.03.127

Geng, H., Yang, J., Dai, Z., Zhang, Y., Zheng, Y., Yu, H., et al. (2017). Co_9S_8/MoS_2 yolk-shell spheres for advanced Li/Na storage. *Small* 13, 201603490. doi:10.1002/smll.201603490

Guo, S., Zhang, P., Feng, Y., Wang, Z., Li, X., and Yao, J. (2020). Rational design of interlaced Co_9S_8/carbon composites from ZIF-67/cellulose nanofibers for enhanced lithium storage. *J. Alloys Compd.* 818, 152911. doi:10.1016/j.jallcom.2019.152911

Han, Y., Li, W., Zhou, K., Wu, X., Wu, H., Wu, X., et al. (2020). Bimetallic sulfide Co_9S_8/N-C@MoS_2 dodecahedral heterogeneous nanocages for boosted Li/K storage. *Chemnanomat* 6, 132–138. doi:10.1002/cnma.201900601

Hou, X., Zhang, Y., Dong, Q., Hong, Y., Liu, Y., Wang, W., et al. (2018). Metal organic framework derived core-shell structured Co_9S_8@N-C@MoS_2 nanocubes for supercapacitor. *ACS Appl. Energy Mat.* 1, 3513–3520. doi:10.1021/acsaem.8b00773

Hu, X., Li, Y., Zeng, G., Jia, J., Zhan, H., and Wen, Z. (2018). Three-dimensional network architecture with hybrid nanocarbon composites supporting few-layer MoS_2 for lithium and sodium storage. *Acs Nano* 12, 1592–1602. doi:10.1021/acsnano.7b08161

Huang, Y., Hu, X., Li, J., Zhang, J., Cai, D., Sa, B., et al. (2020). Rational construction of heterostructured core-shell Bi_2S_3@Co_9S_8 complex hollow particles toward high-performance Li- and Na-ion storage. *Energy Storage Mat.* 29, 121–130. doi:10.1016/j.ensm.2020.04.004

Huang, S., Jin, Z., Ding, Y., Ning, P., Chen, Q., Fu, J., et al. (2021). Encapsulating Fe_2O_3 nanotubes into carbon-coated Co_9S_8 nanocages derived from a MOFs-directed strategy for efficient oxygen evolution reactions and Li-ions storage. *Small* 17, 2103178. doi:10.1002/smll.202103178

Jiang, H., Ren, D., Wang, H., Hu, Y., Guo, S., Yuan, H., et al. (2015). 2D monolayer MoS_2-carbon interoverlapped superstructure: Engineering ideal atomic interface for lithium ion storage. *Adv. Mat.* 27, 3687–3695. doi:10.1002/adma.201501059

Ke, G., Chen, H., He, J., Wu, X., Gao, Y., Li, Y., et al. (2021). Ultrathin MoS_2 anchored on 3D carbon skeleton containing SnS quantum dots as a high-performance anode for advanced lithium ion batteries. *Chem. Eng. J.* 403, 126251. doi:10.1016/j.cej.2020.126251

Kim, M., Anjum, M. A. R., Choi, M., Jeong, H. Y., Choi, S. H., Park, N., et al. (2020). Covalent 0D-2D heterostructuring of Co_9S_8-MoS_2 for enhanced hydrogen evolution in all pH electrolytes. *Adv. Funct. Mat.* 30, 2002536. doi:10.1002/adfm.202002536

Lei, X., Yu, K., Qi, R., and Zhu, Z. (2018). Fabrication and theoretical investigation of MoS_2-Co_3S_4 hybrid hollow structure as electrode material for lithium-ion batteries and supercapacitors. *Chem. Eng. J.* 347, 607–617. doi:10.1016/j.cej.2018.04.154

Li, H., Qian, X., Xu, C., Huang, S., Zhu, C., Jiang, X., et al. (2017). Hierarchical porous Co_9S_8/nitrogen-doped carbon@MoS_2 polyhedrons as pH universal electrocatalysts for highly efficient hydrogen evolution reaction. *ACS Appl. Mat. Interfaces* 9, 28394–28405. doi:10.1021/acsami.7b06384

Li, J., Han, L., Zhang, X., Sun, H., Liu, X., Lu, T., et al. (2021). Multi-role TiO_2 layer coated carbon@few-layered MoS2 nanotubes for durable lithium storage. *Chem. Eng. J.* 406, 126873. doi:10.1016/j.cej.2020.126873

Liu, H., Su, D., Zhou, R., Sun, B., Wang, G., and Qiao, S. Z. (2012). Highly ordered mesoporous MoS_2 with expanded spacing of the (002) crystal plane for ultrafast lithium ion storage. *Adv. Energy Mat.* 2, 970–975. doi:10.1002/aenm.201200087

Liu, J., Wu, C., Xiao, D., Kopold, P., Gu, L., van Aken, P. A., et al. (2016). MOF-derived hollow Co_9S_8 nanoparticles embedded in graphitic carbon nanocages with superior Li-ion storage. *Small* 12, 2354–2364. doi:10.1002/smll.201503821

Lu, Y., Yao, X., Yin, J., Peng, G., Cui, P., and Xu, X. (2015). MoS_2 nanoflowers consisting of nanosheets with a controllable interlayer distance as high-performance lithium ion battery anodes. *RSC Adv.* 5 (11), 7938–7943. doi:10.1039/c4ra14026E

Maksoud, M. I. A. A., Bedir, A. G., Bekhit, M., Abouelela, M. M., Fahim, R. A., Awed, A. S., et al. (2021). MoS_2-based nanocomposites: Synthesis, structure, and applications in water remediation and energy storage: A review. *Environ. Chem. Lett.* 19, 3645–3681. doi:10.1007/s10311-021-01268-x

Miao, Y. J., Zheng, Y. F., Tao, F., Chen, Z. J., Xiong, Y., Ren, F. Z., et al. (2022). Synthesis and application of single-atom catalysts in sulfur cathode for high-performance lithium–sulfur batteries. *Chin. Chem. Lett.* doi:10.1016/j.cclet.2022.01.014

Ren, H., Gu, C., Zhao, J., Joo, S. W., and Huang, J. (2019). Co_9S_8@MoS_2 core-shell nanostructure anchored on reduced graphene oxide with improved electrochemical performance for lithium-ion batteries. *Appl. Surf. Sci.* 473, 918–927. doi:10.1016/j.apsusc.2018.12.257

Ru, J., He, T., Chen, B., Feng, Y., Zu, L., Wang, Z., et al. (2020). Covalent assembly of MoS_2 nanosheets with SnS nanodots as linkages for lithium/sodium-ion batteries. *Angew. Chem. Int. Ed.* 59, 14621–14627. doi:10.1002/anie.202005840

Tao, F., Liu, Y., Ren, X. Y., Jiang, A. J., Wei, H. J., Zhai, X. L., et al. (2021). Carbon nanotube-based nanomaterials for high-performance sodium-ion batteries: Recent advances and perspectives. *J. Alloys Compd.* 873, 159742. doi:10.1016/j.jallcom.2021.159742

Teng, Y., Zhao, H., Zhang, Z., Li, Z., Xia, Q., Zhang, Y., et al. (2016). MoS_2 nanosheets vertically grown on graphene sheets for lithium-ion battery anodes. *ACS Nano* 10 (9), 8526–8535. doi:10.1021/acsnano.6b03683

Tu, C., Peng, A., Zhang, Z., Qi, X., Zhang, D., Wang, M., et al. (2021). Surface-seeding secondary growth for CoO@Co_9S_8 P-N heterojunction hollow nanocube encapsulated into graphene as superior anode toward lithium ion storage. *Chem. Eng. J.* 425, 130648. doi:10.1016/j.cej.2021.130648

Wang, J., Liu, J., Chao, D., Yan, J., Lin, J., and Shen, Z. X. (2014). Self-assembly of honeycomb-like MoS_2 nanoarchitectures anchored into graphene foam for enhanced lithium-ion storage. *Adv. Mat.* 26, 7162–7169. doi:10.1002/adma.201402728

Wang, Y., Yu, L., and Lou, X. W. (2016). Synthesis of highly uniform molybdenum-glycerate spheres and their conversion into hierarchical MoS_2 hollow nanospheres for lithium-ion batteries. *Angew. Chem. Int. Ed.* 55, 7423–7426. doi:10.1002/anie.201601673

Wang, S., Guan, B. Y., Yu, L., and Lou, X. W. (2017). Rational design of three-layered TiO_2@Carbon@MoS_2 hierarchical nanotubes for enhanced lithium storage. *Adv. Mat.* 29, 1702724. doi:10.1002/adma.201702724

Wang, J., He, H., Wu, Z., Liang, J., Han, L., Xin, H. L., et al. (2018a). Controllable construction of flower-like FeS/Fe_2O_3 composite for lithium storage. *J. Power Sources* 392, 193–199. doi:10.1016/j.jpowsour.2018.04.107

Wang, Y., Kang, W., Cao, D., Zhang, M., Kang, Z., Xiao, Z., et al. (2018b). A yolk-shelled Co_9S_8/MoS_2-CN nanocomposite derived from a metal-organic framework as a high performance anode for sodium ion batteries. *J. Mat. Chem. A* 6, 4776–4782. doi:10.1039/c8ta00493e

Wang, F., Liu, Y., Wei, H.-J., Li, T.-F., Xiong, X.-H., Wei, S. Z., et al. (2021). Recent advances and perspective in metal coordination materialsbased electrode materials for potassium-ion batteries. *Rare Met.* 40 (2), 448–470. doi:10.1007/s12598-020-01649-1

Wu, T., Jing, M., Liu, Y., and Ji, X. (2019). Binding low crystalline MoS_2 nanoflakes on nitrogen-doped carbon nanotube: Towards high-rate lithium and sodium storage. *J. Mat. Chem. A* 7, 6439–6449. doi:10.1039/c9ta00123a

Xie, D., Xia, X., Wang, Y., Wang, D., Zhong, Y., Tang, W., et al. (2016). Nitrogen-doped carbon embedded MoS_2 microspheres as advanced anodes for lithium- and sodium-ion batteries. *Chem. Eur. J.* 22 (33), 11617–11623. doi:10.1002/chem.201601478

Yang, Q., Lu, R., Ren, S., Chen, C., Chen, Z., and Yang, X. (2018). Three dimensional reduced graphene oxide/ZIF-67 aerogel: Effective removal cationic and anionic dyes from water. *Chem. Eng. J.* 348, 202–211. doi:10.1016/j.cej.2018.04.176

Yang, K., Mei, T., Chen, Z., Xiong, M., Wang, X., Wang, J., et al. (2020). Chinese hydrangea lantern-like Co_9S_8@MoS_2 composites with enhanced lithium-ion battery properties. *Nanoscale* 12, 3435–3442. doi:10.1039/c9nr09260a

Yu, X.-Y., Hu, H., Wang, Y., Chen, H., and Lou, X. W. (2015). Ultrathin MoS_2 nanosheets supported on N-doped carbon nanoboxes with enhanced lithium storage and electrocatalytic properties. *Angew. Chem. Int. Ed.* 54, 7395–7398. doi:10.1002/anie.201502117

Zhang, L., and Lou, X. W. (2014). Hierarchical MoS_2 shells supported on carbon spheres for highly reversible lithium storage. *Chem. Eur. J.* 20 (18), 5219–5223. doi:10.1002/chem.201400128

Zhang, S., Chowdari, B. V. R., Wen, Z., Jin, J., and Yang, J. (2015). Constructing highly oriented configuration by few-layer MoS_2: Toward high-performance lithium-ion batteries and hydrogen evolution reactions. *Acs Nano* 9, 12464–12472. doi:10.1021/acsnano.5b05891

Zhang, X., Zhao, R., Wu, Q., Li, W., Shen, C., Ni, L., et al. (2017). Petal-like MoS_2 nanosheets space-confined in hollow mesoporous carbon spheres for enhanced lithium storage performance. *Acs Nano* 11, 8429–8436. doi:10.1021/acsnano.7b04078

Zhang, Z., Zhao, H., Teng, Y., Chang, X., Xia, Q., Li, Z., et al. (2018). Carbon-sheathed MoS_2 nanothorns epitaxially grown on CNTs: Electrochemical application for highly stable and ultrafast lithium storage. *Adv. Energy Mat.* 8, 1700174. doi:10.1002/aenm.201700174

Zhao, B., Wang, Z., Gao, Y., Chen, L., Lu, M., Jiao, Z., et al. (2016). Hydrothermal synthesis of layer-controlled MoS_2/graphene composite aerogels for lithium-ion battery anode materials. *Appl. Surf. Sci.* 390, 209–215. doi:10.1016/j.apsusc.2016.08.078

Zhao, Y., Bi, M., Qian, F., Zeng, P., Chen, M., Wang, R., et al. (2018). Heterostructure CoS/NC@MoS_2 hollow spheres for high-performance hydrogen evolution reactions and lithium-ION batteries. *Chemelectrochem* 5, 3953–3960. doi:10.1002/celc.201801166

Zhao, R., Han, Y., Li, W., Li, J., Chen, M., and Chen, L. (2020). Construction of nanocage-structured heterogeneous binary metal sulfides via step-by-step confined growth for boosted lithium storage properties. *Chem. Commun.* 56, 6798–6801. doi:10.1039/d0cc00962h

Zhou, F., Xin, S., Liang, H.-W., Song, L.-T., and Yu, S.-H. (2014). Carbon nanofibers decorated with molybdenum disulfide nanosheets: Synergistic lithium storage and enhanced electrochemical performance. *Angew. Chem. Int. Ed.* 53, 11552–11556. doi:10.1002/anie.201407103

Zhou, J., Qin, J., Zhang, X., Shi, C., Liu, E., Li, J., et al. (2015a). 2D space-confined synthesis of few-layer MoS_2 anchored on carbon nanosheet for lithium-ion battery anode. *Acs Nano* 9, 3837–3848. doi:10.1021/nn506850e

Zhou, Y., Yan, D., Xu, H., Feng, J., Jiang, X., Yue, J., et al. (2015b). Hollow nanospheres of mesoporous Co_9S_8 as a high-capacity and long-life anode for advanced lithium ion batteries. *Nano Energy* 12, 528–537. doi:10.1016/j.nanoen.2015.01.019